The Astrophysical Journal, 998:285 (13pp), 2026 February 20 https://doi.org/10.3847/1538-4357/ae3824
© 2026. The Author(s). Published by the American Astronomical Society.
OPEN ACCESS

JWST Reveals a Candidate Jellyfish Galaxy at $z = 1.156$

Ian D. Roberts[1,2], Michael L. Balogh[1,2], Visal Sok[3], Adam Muzzin[3], Michael J. Hudson[1,2,4], and Pascale Jablonka[5]
[1] Department of Physics & Astronomy, University of Waterloo, Waterloo, ON N2L 3G1, Canada; ianr@uwaterloo.ca
[2] Waterloo Centre for Astrophysics, University of Waterloo, 200 University Avenue West, Waterloo, ON N2L 3G1, Canada
[3] Department of Physics and Astronomy, York University, 4700 Keele Street, Toronto, ON M3J 1P3, Canada
[4] Perimeter Institute for Theoretical Physics, 31 Caroline Street North, Waterloo, ON N2L 2Y5, Canada
[5] Laboratoire d'astrophysique, École Polytechnique Fédérale de Lausanne (EPFL), CH-1290 Sauverny, Switzerland
Received 2025 June 16; revised 2026 January 5; accepted 2026 January 11; published 2026 February 17

Abstract

We report the discovery of COSMOS2020-635829 as a candidate jellyfish galaxy undergoing ram pressure stripping in a (proto)cluster at $z > 1$. High-resolution imaging from the James Webb Space Telescope reveals a symmetric stellar disk coupled to a unilateral tail of star-forming knots to the south. Using Gemini GMOS integral field unit (IFU) observations, we show that these extraplanar continuum sources are embedded within an ionized gas tail that is kinematically connected to the disk of COSMOS2020-635829. If confirmed, this represents the highest-redshift discovery of a ram-pressure stripped ionized gas tail. The tail sources are characterized by extremely young stellar populations ($\lesssim$100 Myr), have stellar masses of $\sim 10^8\,M_\odot$, and star formation rates of 0.1–1 $M_\odot\,\mathrm{yr}^{-1}$. This work shows that ram-pressure stripping can potentially perturb group and cluster galaxies at $z > 1$ and may contribute to environmental quenching even near Cosmic Noon.

Unified Astronomy Thesaurus concepts: Galaxy evolution (594); Galaxy spectroscopy (2171); Galaxy tails (2125); High-redshift galaxy clusters (2007); Star formation (1569); Ram pressure stripped tails (2126); Galaxy groups (597); Galaxy clusters (584)

1. Introduction

For approximately 50 yr it has been known, at least to some degree, that the properties of galaxies in overdense environments like galaxy groups and clusters differ systematically from those relatively isolated in the field. This dichotomy is reflected in a number of galaxy properties, but among the most studied is the overabundance of red, quiescent satellite galaxies in dense environments (e.g., A. Dressler 1980; M. Postman et al. 2005; M. R. Blanton & J. Moustakas 2009; Y.-j. Peng et al. 2010; A. R. Wetzel et al. 2012; D. J. Wilman & P. Erwin 2012; C. P. Haines et al. 2015; I. D. Roberts & L. C. Parker 2017). This "environmental quenching" of galaxies is strongest in the most massive galaxy clusters with the fraction of quiescent galaxies approaching the field value for the lowest-mass galaxy groups (e.g., T. Kimm et al. 2009; A. R. Wetzel et al. 2012).

The origins of this quenching have been attributed to a suite of physical mechanisms that are unique to dense environments (see L. Cortese et al. 2021, for a recent review), the most commonly invoked being the cessation of cold-gas accretion onto satellite galaxies (often referred to as "starvation" or "strangulation"), either due to the high virial temperature of the group or cluster halo, or due to the circumgalactic medium being stripped off of the galaxy (e.g., R. B. Larson et al. 1980; M. L. Balogh et al. 1999; Y. Peng et al. 2015); or the direct stripping of cold gas from galaxies, either due to ram-pressure stripping (RPS; e.g., J. E. Gunn & J. R. Gott 1972; G. Gavazzi 1978; G. Gavazzi & W. Jaffe 1987) or from tidal interactions with other group or cluster galaxies that can either directly strip material or tidally stir and heat gas making it more easily removed by ram pressure (e.g., A. Boselli & G. Gavazzi 2006; L. Mayer et al. 2006). It is likely that the effectiveness of these various environmental perturbations depends on the mass of the host halo. For example, ram-pressure strength scales with the density of, and velocity relative to, the intracluster medium (ICM) as $\rho_{\mathrm{ICM}}v^2$, and thus will be strongest in massive galaxy clusters. Conversely, tidal interactions and even galaxy mergers will be more common in lower-mass groups where the typical orbital velocities are closer to the escape velocity for two interacting galaxies.

In the low-redshift Universe, a comprehensive understanding of the relative balance between different quenching mechanisms as a function of host environment is still elusive —but progress has been made. It is now clear that RPS plays an important role in quenching galaxies in galaxy clusters. This has been inferred through the need for short quenching times (e.g., V. Quilis et al. 2000; A. Muzzin et al. 2014), observed signatures of outside-in quenching (e.g., L. Cortese et al. 2012; A. L. Schaefer et al. 2017, 2019; R. A. Finn et al. 2018; M. S. Owers et al. 2019; C. R. Morgan et al. 2024; A. O. Broderick et al. 2025), as well as the identification of so-called "jellyfish" galaxies with one-sided tails of stripped interstellar medium that extend well beyond the main galaxy disk (e.g., G. Gavazzi & W. Jaffe 1987; G. Gavazzi et al. 2001; A. Chung et al. 2007; B. M. Poggianti et al. 2017; A. Boselli et al. 2018; I. D. Roberts et al. 2021b, 2022a; A. Ignesti et al. 2023). In lower-mass galaxy groups, the picture is less clear. RPS certainly does occur in such halos (e.g., M. Bureau & C. Carignan 2002; J. Rasmussen et al. 2006; A. W. McConnachie et al. 2007; D. Hu et al. 2024; I. D. Roberts et al. 2024; R. A. Finn et al. 2025), but the frequency is lower (I. D. Roberts et al. 2021a). Even in the most massive clusters, it is unlikely that ram pressure is responsible for stripping all (or even most) of the molecular gas in satellite galaxies (e.g., N. Zabel et al. 2022; T. Brown et al. 2023; A. B. Watts et al. 2023). Instead,

Original content from this work may be used under the terms of the Creative Commons Attribution 4.0 licence. Any further distribution of this work must maintain attribution to the author(s) and the title of the work, journal citation and DOI.

quenching likely operates in conjunction with gas depletion (which is then not replenished) from star formation, both prior to galaxies reaching the inner regions of groups and clusters where RPS is efficient, and after gas disks are truncated by ram pressure in order to "finish off" quenching. This has recently been framed as the "slow-then-rapid" quenching paradigm where this interplay between starvation and strangulation and RPS drives the quenched fractions in low-redshift clusters (A. R. Wetzel et al. 2013; R. F. J. van der Burg et al. 2018; C. Maier et al. 2019; I. D. Roberts et al. 2019; A. Manuwal & A. R. H. Stevens 2023; C. R. Morgan et al. 2024; A. O. Broderick et al. 2025).

At higher redshift ($z \sim 1$–2), far less is known. It has been shown that cluster red sequences in excess of the field population are in place in dense environments at these redshifts (e.g., A. Muzzin et al. 2012; P. Cerulo et al. 2016; L. J. Old et al. 2020). This, in and of itself, implies that relatively short quenching timescales are needed given the limited time available for group and cluster formation and subsequent environmental quenching at high z. Direct evidence for RPS at high redshift is limited due to both the required sensitivity to detect the typically faint morphological signatures of RPS and the required angular resolution for spatially resolving them. Of the examples in literature, A. G. Noble et al. (2019) present marginally resolved molecular gas extensions in $z \sim 1.6$ cluster galaxies that may represent RPS tails. More recently, K. Xu et al. (2025) report molecular gas observations of galaxies in a $z = 2.51$ protocluster, at least three of which show some compelling evidence for one-sided tails, potentially driven by ram pressure.

The bulk of galaxies on the cluster red sequence at $z \sim 0$ ceased substantial star formation at $z \gtrsim 1$–2 (e.g., T. Kodama & N. Arimoto 1997; R. de Propris et al. 1999; C. L. Mancone et al. 2010). Thus a key avenue for understanding the quenched population in the local Universe is to observe environmental quenching mechanisms, such as RPS, in action at high z. In the local Universe, ionized gas tails are among the most frequently identified signatures of RPS (e.g., M. Yagi et al. 2010; B. M. Poggianti et al. 2017; A. Boselli et al. 2018), but to date no examples of RPS ionized gas tails have been identified beyond $z = 0.7$ (A. Boselli et al. 2019). Identifying analogous galaxies at high redshift (to the extent that they exist) must be a fruitful path for advancing our knowledge of environmental quenching. Currently the number of known, unquestionable examples of RPS at $z > 1$ is likely zero, and the number of jellyfish galaxy candidates in the present literature is almost certainly <10. Any new identification of such objects is thus an important addition.

In this work we present COSMOS2020-635829 ($\alpha = 149.81480$, $\delta = 2.02811$), a new candidate for a satellite galaxy at $z = 1.156$ undergoing active RPS. COSMOS2020-635829 is associated with a cluster-mass, X-ray-detected overdensity and shows a one-sided collection of blue, extraplanar knots that are cospatial with an ionized gas tail. This is among the strongest candidates for a jellyfish galaxy at $z > 1$, and if said interpretation is correct, the current highest redshift example of an RPS ionized gas tail as well extraplanar star formation.

The outline of the paper is as follows. In Section 2 we introduce the data products used in this work, including broadband imaging (James Webb Space Telescope (JWST), Hubble Space Telescope (HST), and Subaru) as well as spatially resolved spectroscopy (Gemini). In Section 3 we provide an outline of COSMOS2020-635829's status as a jellyfish galaxy candidate based on rest-frame optical and near-IR imaging. In Section 4 we present the detection of an ionized gas tail to the south of COSMOS2020-635829 that is cospatial with the observed rest-frame optical asymmetries. In Section 5 we present an analysis of the ongoing star formation in the extraplanar sources, presumed to be fueled by RPS gas. Finally, in Sections 6 and 7 we discuss the key results from this work as well as make concluding remarks. Throughout, we assume a flat ΛCDM cosmology with $\Omega_M = 0.3$, $\Omega_\Lambda = 0.7$, and $H_0 = 70\,\mathrm{km\,s^{-1}\,Mpc^{-1}}$.

2. Data

2.1. Broadband Imaging

Our primary imaging source for this work is publicly available, multiband JWST imaging of the COSMOS field from the COSMOS-Web Survey (C. M. Casey et al. 2023; M. Franco et al. 2025). This is from COSMOS-Web Data Release 0.5 which includes $\sim 0.3\,\mathrm{deg}^2$ of the COSMOS field in the NIRCam F115W, F150W, F277W, and F444W filters. A far smaller area is also covered by the MIRI F770W filter, though this does not cover COSMOS2020-635829. This JWST imaging was used to first identify COSMOS2020-635829 as a jellyfish galaxy candidate (see Section 3; I. D. Roberts et al. 2026, in preparation). We also make use of HST F814W imaging (A. M. Koekemoer et al. 2011) and deconvolved Subaru Suprime-Cam *B*-, *V*-, *r*-, and *z*-band imaging (V. Sok et al. 2022) in Section 5 for spectral energy distribution (SED) fitting. Finite-resolution deconvolution is applied to the deep Suprime-Cam imaging of the COSMOS field to achieve an angular resolution of $0\farcs3$; this procedure is described in detail by V. Sok et al. (2022). The JWST and HST data described above may be obtained from the MAST archive via A. Faisst (2024) and N. Scoville (2006).

2.2. GMOS Spectroscopy

We observed COSMOS2020-635829 with the GMOS integral field unit (IFU) in the 2025A semester (PI: I. D. Roberts; program code GN-2025A-FT-205). We used the single-slit GMOS IFU with a central wavelength of 8900 Å (with ±100 Å spectral dithers) and the R400 grating. This gives a field of view (FOV) of $\sim 3\farcs5 \times 5''$ and a spectral resolution of $R = 3000$ ($\sigma_{\mathrm{inst}} \simeq 43\,\mathrm{km\,s^{-1}}$). Our main target is the redshifted [O II] λλ3726, 3729 emission line doublet, which is among the brightest observable emission lines in the rest-frame optical spectrum. The Hα line is not observable from the ground for COSMOS2020-635829 as it falls between the *J* and *H* atmospheric windows. We observed COSMOS2020-635829 for a total integration time of 5 hr, which was split over three nights (2025 March 02, 2025 April 21, and 2025 May 26) in observing blocks of 5×1200 s, each bracketed by flat-field and CuAr arc observations. The standard star EG131 was also observed for spectrophotometric calibration. For the three nights the raw image quality during our observations was 70th percentile, 70th percentile, 20th percentile, respectively, and the average airmass was 1.2, 1.5, and 1.5, respectively.

Data reduction was done using the Gemini IRAF software package following the GMOS IFU-1 data reduction tutorial.[6]

[6] gmos-ifu-1-data-reduction-tutorial-gemini-iraf.readthedocs.io/en/latest/index.html

The standard reduction steps were completed, including bias and overscan correction, flat-fielding, scattered light removal, cosmic-ray rejection, and sky subtraction. We use our standard star observation for flux calibration, and we further refine our flux scale using the calibrated DESI Data Release 1 spectrum of COSMOS2020-635829. A calibrated data cube was produced for each 1200 s science exposure, with pixel sizes of $0\farcs1$ in the spatial directions and 0.76 Å in the spectral direction. The cubes were then reprojected onto a common wavelength grid and coadded with inverse-variance weighting to produce our final science cube. In the vicinity of the [O II] doublet, we achieve a 1σ sensitivity of $\lesssim 10^{-18}$ erg s^{-1} cm^{-2} Å^{-1} arcsec^{-1}.

3. COSMOS2020-635829: A Jellyfish Galaxy Candidate at $z > 1$

COSMOS2020-635829 is a an intermediate-mass ($M_{\rm star} \sim 10^{10}\,M_{\odot}$), strongly star-forming (star formation rate (SFR) $\sim 100\,M_{\odot}\,{\rm yr}^{-1}$) galaxy at a redshift of $z_{\rm spec} = 1.1560$ (J. R. Weaver et al. 2022; DESI Collaboration et al. 2024). It was initially flagged as a jellyfish galaxy candidate by I. D. Roberts et al. (2026, in preparation) based on high-resolution rest-frame optical and near-IR imaging from the JWST COSMOS-Web survey (C. M. Casey et al. 2023). This selection of jellyfish galaxy candidates at $z \gtrsim 1$ will be outlined in detail by I. D. Roberts et al. (2026, in preparation), but in brief, galaxies were selected according to one or more of the following morphological features.

1. A one-sided extension in the stellar distribution, which is interpreted as being in the direction of a potential RPS tail. This extension may be associated with unwinding spiral arms (e.g., C. Bellhouse et al. 2021), but it does not need to be.
2. A one-sided collection of knots that are detached from the main stellar distribution of the galaxy. We require that these knots are similar in color to at least some part of the main galaxy, in order to reduce the odds of background sources in projection.
3. Evidence for enhanced star formation on the proposed leading edge. We require this to be in conjunction with a proposed tail direction from one of the above features. This means that a galaxy that shows apparently asymmetric star formation within its disk, but no sign of a one-sided extension, will not be classified as a jellyfish galaxy candidate. Signs of enhanced star formation on the leading edge may be used to classify a galaxy as a jellyfish galaxy candidate with only marginal evidence for a "tail" extension, if the orientation of the potential enhanced star formation and tail direction are mutually consistent.

This is analogous to the visual selections of ram-pressure candidates that have become relatively common, and quite successful, at $z \sim 0$ (H. Ebeling et al. 2014; B. M. Poggianti et al. 2016; I. D. Roberts & L. C. Parker 2020; F. Durret et al. 2021; I. D. Roberts et al. 2022b; J. P. Crossett et al. 2025). In this framework the direction of the one-sided extension is interpreted as the direction of a potential ram-pressure tail. We stress that these visual selections will by no means identify a pure sample of galaxies undergoing RPS, as there are other physical processes (e.g., tidal effects) that can perturb galaxies in groups and clusters, but through follow-up observations and analyses we can hope to confirm some fraction of these candidates.

In Figure 1 we show single-band images of COSMOS2020-635829 in the four COSMOS-Web filters as well as a color composite. The morphology of COSMOS2020-635829 is given by a symmetric main galaxy component coupled to compact, relatively blue, knots distributed to the south of the galaxy. It is these knots for which COSMOS2020-635829 was selected as a ram-pressure candidate under the assumption that they may correspond to sites of extraplanar star formation within an RSP gaseous tail (i.e., criteria 1 and 2). While at first glance these knots appear largely detached from the main galaxy disk, close inspection (particularly of the F115W and F150W imaging) shows that they are connected to the main disk through faint emission that appears to extend from spiral arms in the main galaxy. The F115W (rest-frame near-UV) is also brighter on the leading half than the trailing half of COSMOS2020-635829, and thus possibly also satisfying criterion 3, though this was not a feature on which COSMOS2020-635829 was initially selected. The four tail sources are highlighted in the color composite in Figure 1 and will be the subject of further investigation in Section 5.

The ram-pressure candidates from I. D. Roberts et al. (2026, in preparation) are selected without knowledge of the environments within which the galaxies reside, but it is found postclassification that the identified ram-pressure candidates are preferentially associated with overdense environments. COSMOS2020-635829 is no exception. In Figure 2 we show the 2D galaxy density distribution for galaxies within $10'$ of COSMOS2020-635829 and with $1.0 < z_{\rm phot} < 1.3$. COSMOS2020-635829 is associated with a complex and extended overdensity. The galaxy is spatially coincident with an $\sim$2–3 $\times\ 10^{13}\,M_{\odot}$ halo at $z_{\rm phot} \sim 1.23$, as identified by the AMICO cluster finding algorithm (G. Toni et al. 2024). This halo also appears at the outskirts of a strong galaxy overdensity centered on two halos in the AMICO-COSMOS catalog with photo-zs of 1.15 and 1.29, each X-ray detected at $\sim 4\sigma$, and with a combined halo mass of $\sim 10^{14}\,M_{\odot}$.

The closest galaxy companion to COSMOS2020-635829 (with $1.0 < z_{\rm phot} < 1.3$) has a projected physical separation of $\sim$75 kpc (J. R. Weaver et al. 2022), though this galaxy does not have a measured spectroscopic redshift. The closest neighbor with a spectroscopic redshift and within 1000 km s^{-1} of COSMOS2020-635829 is at a projected physical separation of 1200 kpc (A. A. Khostovan et al. 2026). While we cannot fully rule out a tidal origin for the observed morphology of COSMOS2020-635829, this shows that it does not currently have any close tidal companions. There is always the possibility of a past tidal interaction with a satellite that is no longer in the vicinity of COSMOS2020-635829. Stellar tidal tails should have colors that are similar to the host galaxy, particularly the outskirts of the host galaxy where stars are most easily unbound. In Figure 3 we plot the F115W – F444W color profile[7] for the main disk of COSMOS2020-635829 compared to the tail (both for individual sources and integrated over the tail region). The color profile is extracted in $0\farcs1$ circular annuli from the galaxy center out the the edge of the disk ($\sim 1''$). The color of the tail is clearly bluer than all regions of the main disk, thus inconsistent with the stellar emission in the tail resulting from simple tidal stripping.

[7] We note that the trend in Figure 3 is not sensitive to the filter combination that we use to measure the galaxy and tail colors.

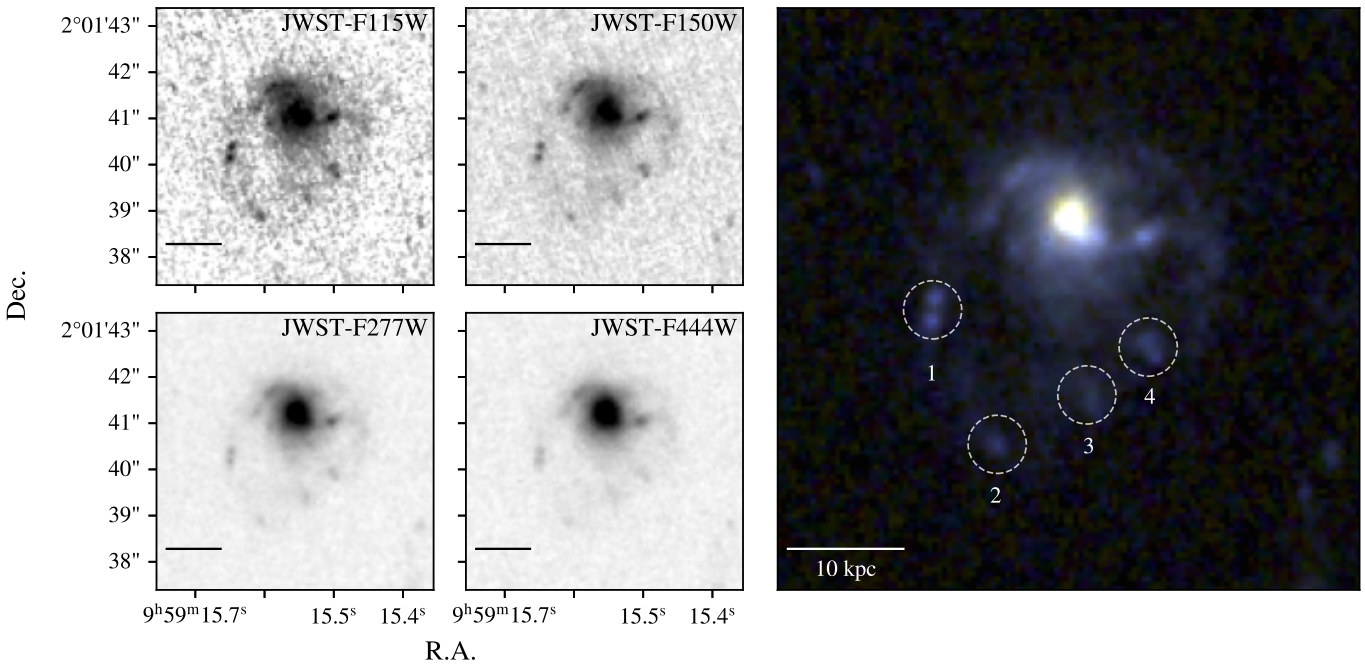

Figure 1. Thumbnail images of COSMOS2020-635829 for the four JWST filters used in this work. The red–green–blue image on the right is a combination of JWST F444W (red channel), F277W (green channel), and F115W + F150W (blue channel). The dashed circles mark the four extraplanar sources that are identified in the tail of COSMOS2020-635829.

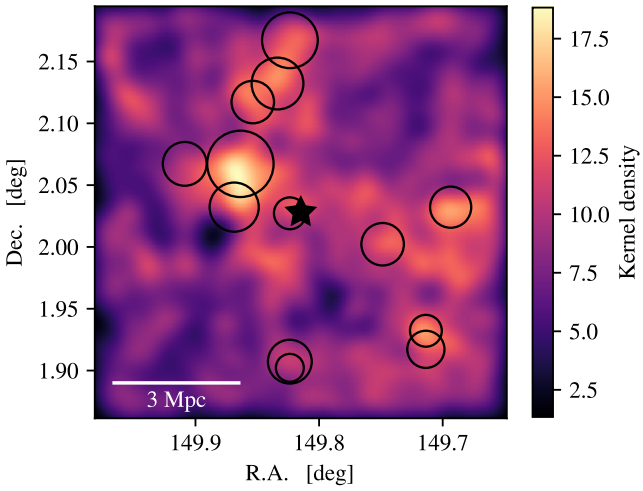

Figure 2. Large-scale structure around COSMOS2020-635829. The large star marks the position of COSMOS2020-635829. The color map shows a 2D kernel density estimate of all galaxies from the COSMOS2020 catalog within 10′ of COSMOS2020-635829 and with $1.0 < z_{\rm phot} < 1.3$. Open circles correspond to groups or clusters from the AMICO-COSMOS catalog within 10′ of COSMOS2020-635829 and with $1.0 < z_{\rm phot} < 1.3$.

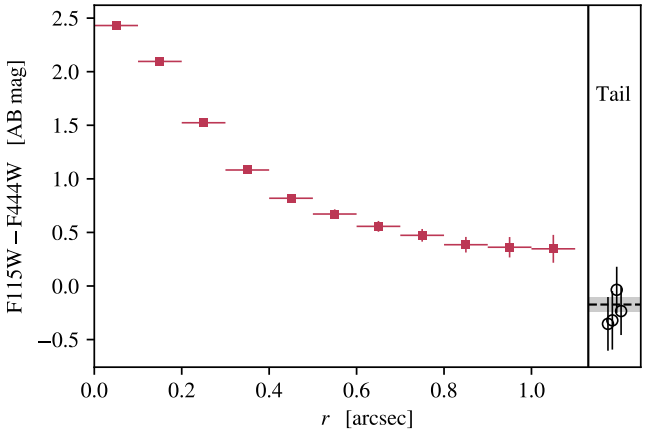

Figure 3. Color profile for the main disk of COSMOS2020-635829 measured in circular annuli from the galaxy center to the edge of the disk. Vertical error bars show the 1σ statistical uncertainties on the measured color; horizontal error bars show the annuli widths. The far right of the figure shows the color in the tail region, both integrated over the full tail (dashed line) as well as measured individually for the tail sources highlighted in Figure 1.

We cannot rule out the possibility that gas is tidally stripped from COSMOS2020-635829, which then proceeds to form stars in situ in the tail, but gas being tidally stripped without strongly distorting the stellar distribution seems unlikely. Conversely, a stellar tail which is bluer than the main galaxy is exactly what is expected from star formation within an RPS tail. An additional possibility is that COSMOS2020-635829 is a collisional ring galaxy and the observed blue star-forming sources are part of a circumgalactic star-forming ring. We table further discussion of this possibility for now and leave it to be addressed comprehensively in Section 6.1. Ultimately, given the data in hand we cannot entirely rule out this possibility, or the tidal stripping scenario for that matter, but we do favor an RPS origin as the most likely scenario, as we outline in the subsequent sections.

4. Detection of an Ionized Gas Tail

The association with an overdense environment is a necessary but insufficient condition for establishing COSMOS2020-635829 as a jellyfish galaxy undergoing RPS. Furthermore, the knots in the JWST imaging of COSMOS2020-635829 cannot be definitively associated with the main galaxy through photometry alone. In this section we present the detection of an ionized gas tail to the south of COSMOS2020-635829, spatially coincident with the extraplanar rest-frame optical and near-IR sources. First we perform an aperture analysis in order to demonstrate that extraplanar

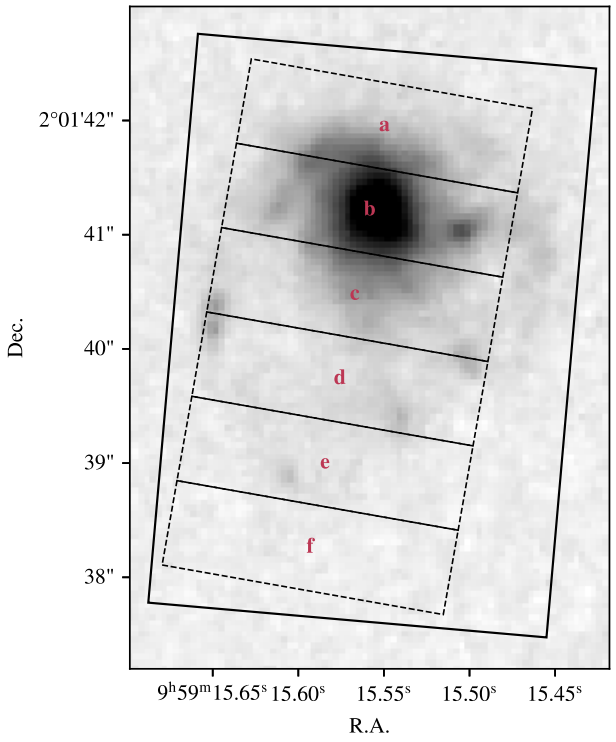

Figure 4. Overlay of the GMOS IFU-1 FOV (solid box) on top of the JWST F277W image of COSMOS2020-635829. In the dashed boxes we show the apertures along the proposed tail direction that are used for extracting spectra around the [O II] $\lambda\lambda$3726, 3729 doublet.

ionized gas emission is present along the "tail" direction at a high signal-to-noise ratio (S/N), and second we generate maps of [O II] flux and velocity in order to derive rough constraints on the spatial distribution, given our seeing-limited angular resolution.

4.1. Aperture Analysis

In Figure 4 we show the GMOS IFU FOV (solid line) overlaid on the F277W image of COSMOS2020-635829. We also show six apertures along the tail axis, labeled "a" through "f," which have widths of 2.″5 and heights of 0.″75. The height of 0.″75 corresponds to the FWHM image quality (∼0.″7–0.″8) and the width of 2.″5 is chosen to span the full optical disk of COSMOS2020-635829. A key goal of the GMOS IFU observations of COSMOS2020-635829 is to test for the presence of an ionized gas tail that is cospatial with the inferred ram-pressure tail from broadband imaging. To do so we extract spectra around the [O II] $\lambda\lambda$3726, 3729 lines for each aperture along the tail axis. If a stripped ionized gas tail is present then we should see [O II] emission that extends beyond the main optical disk of the galaxy, and specifically this should be seen to the south of COSMOS2020-635829.

Figure 5 shows these extracted spectra. We fit each spectrum with a model that is a composite of a continuum model and a double-Gaussian model for the [O II] doublet, given by

$$F_\lambda(\lambda) = P(a_0, a_1, \lambda) + \mathcal{N}(A_1, v, \sigma, \lambda) + \mathcal{N}(A_2, v, \sigma, \lambda), \quad (1)$$

where λ is the observed wavelength, P is a first-order polynomial to account for any offset or tilt in the continuum level, and $\mathcal{N}$ are normal distributions with peak fluxes A_1 and A_2 corresponding to the two [O II] lines. We tie both lines in the [O II] doublet to a common velocity (v) and line width (σ). We also set a physically motivated prior range of $0.35 < A_2/A_1 < 1.5$ for the flux ratio between the two [O II] lines (M. V. F. Copetti & B. C. Writzl 2002; A. K. Pradhan et al. 2006). For each extracted spectrum this gives six free parameters. We determine the best-fit parameters using the Markov Chain Monte Carlo package `EMCEE` (D. Foreman-Mackey et al. 2013) with flat priors on all model parameters. Chains are all checked for convergence by ensuring that the number of samples is greater than 50τ, where τ is the chain autocorrelation time (see `EMCEE` documentation).[8]

The best-fit spectral models are shown in Figure 5 in red. We note that the observed spectra and best-fit model in Figure 5 have had the best-fit continuum polynomial subtracted off. The yellow bands in the panels mark regions of the spectra that are masked during fitting due to significant residuals from sky-line subtraction. We calculate the total [O II] flux as

$$F_{[\mathrm{OII}]} = \sqrt{2\pi}\,\sigma(A_1 + A_2). \quad (2)$$

We detect the [O II] doublet in all apertures. This includes detections at separations well beyond the main stellar disk and even beyond the extraplanar sources seen in the JWST imaging. In Figure 6(top) we plot [O II] flux as a function of distance from the galaxy center (dy) in kiloparsecs. We consider the flux profile shown in Figure 6 to be indicative of a detected ionized gas tail to the south of COSMOS2020-635829. The ionized gas emission extends beyond the optical galaxy disk by ∼20 kpc all the way to the edge of the IFU FOV. For reference, in Figure 6(top) we overplot F277W surface-brightness profiles along the "leading" and "trailing" sides of the main disk, as well as the two perpendicular directions. These profiles are measured after convolution to the resolution of the GMOS spectroscopy and are arbitrarily shifted to match the normalization of the [O II] profile. These profiles reflect the symmetric nature of the galaxy disk (there is little to no difference between the different quadrants of the galaxy) and highlight the excess [O II] emission that is present for $dy \gtrsim 10$ kpc.

In Figure 6 (bottom) we show the velocity profile for the detected ionized gas along the tail axis. A clear velocity gradient is observed from the leading side through to the far edge of the tail. This coherence definitively associates this extraplanar ionized gas emission with the main galaxy. It also indirectly indicates that the extraplanar broadband optical and near-IR (rest-frame) emission to the south of COSMOS2020-635829 is also associated with the main galaxy.

4.2. Ionized Gas Maps

To explore the ionized gas emission in the tail region in more detail, we now construct maps of [O II] surface brightness and velocity. To do so we need to consider the limitations of our IFU spectroscopy both in terms of angular resolution and depth. We first bin up the IFU cube from its native pixel scale of 0.″1 to a pixel scale of 0.″4, in order to roughly Nyquist sample the seeing of our data. We then extract spectra from spatial bins that are determined from the PowerBin algorithm—a modern alternative to Voronoi binning

[8] emcee.readthedocs.io/en/stable/tutorials/autocorr/

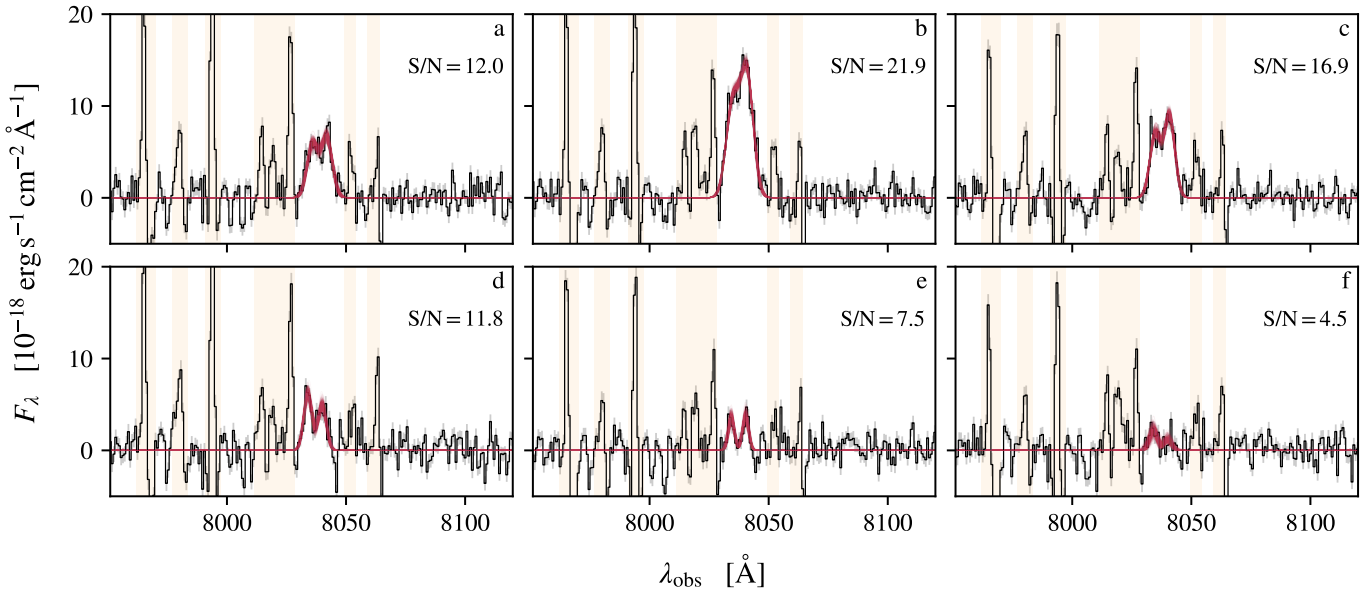

Figure 5. Extracted spectra around the [O II] line for various slices along the tail axis. The labels in each panel correspond to the aperture labels in Figure 4. The black line and shading show the observed spectrum and uncertainty and the red lines show 500 random samples from the posterior distribution for the best-fit double-Gaussian model. These spectra are shown post–continuum subtraction with a first-order polynomial. For each spectrum we list the S/N for the detection of the [O II] doublet. The yellow bands mark regions of the spectrum where significant sky-line residuals are seen, these regions of the spectrum are masked during fitting.

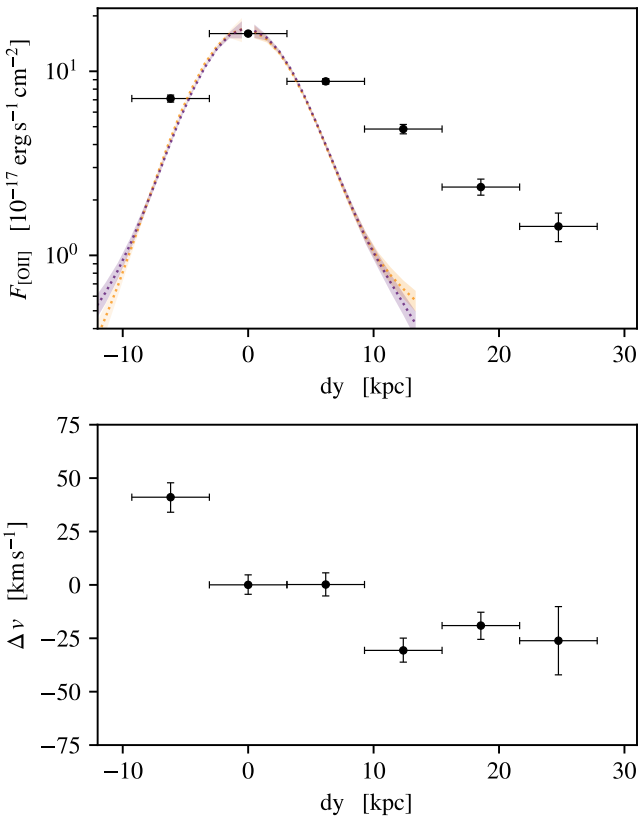

Figure 6. Profiles of [O II] flux (top) and velocity (bottom) along the tail axis; the dashed vertical line marks the center of the galaxy. The y error bars correspond the the 16th and 84th percentiles from the posterior distributions for the spectral fits. The x error bars correspond to the aperture width (see Figure 4). For reference, the colored lines show surface-brightness profiles extracted along four quadrants for the main disk of COSMOS2020-635829. The yellow lines correspond to the "leading" and "trailing" sides along the axis of the tail direction and the purple lines correspond to the two perpendicular quadrants. These profiles have been scaled arbitrarily to match the normalization of the [O II] profile. The velocity profile has been normalized such that $v = 0$ corresponds to the galaxy center.

(M. Cappellari 2025). For each spaxel, we calculate the S/N for the flux measured over an $\sim$500 km s^{-1} window centered on the observed wavelength of the midpoint of the [O II] doublet. We then bin spatially according to a target minimum S/N of five, though many spaxels in the galaxy disk already have an S/N in excess of this target. The binned spectra are fit with an identical model and the procedure outlined in Section 4.1.

In Figure 7 we show the resulting [O II] surface-brightness and velocity maps. We only include spatial bins where the [O II] flux is detected at S/N $>$ 3 and the velocity converges on a unimodal posterior distribution. Furthermore, we visually inspect all of the fits to ensure that they are consistent with the [O II] doublet being fit and that they are not obviously fitting to noise spikes or sky-line residuals. Figure 7 shows that the ionized gas emission is not limited just to the stellar sources visible in the JWST imaging, but instead fills the full region to the south of COSMOS2020-635829. Qualitatively, the diffuse [O II] surface brightness falls off steadily in the $-y$-direction beyond the galaxy disk, and there is no clear structure (gradient or otherwise) across the tail in the x-direction. These facts are supported quantitatively by the surface-brightness profiles along the x- and y-directions shown in Figure 7. For the surface-brightness profile along the x-direction we have removed the gradient along the y-direction in order to align each spatial bin to a common normalization. The slope of the best-fit profile along the y-direction is positive whereas the gradient along the x-direction is consistent with zero.

Kinematically, the ionized gas in the disk follows a pattern of ordered rotation. There is some evidence that signatures of this rotation pattern are also present in the extraplanar gas to the south, though the spatial bins become large and the structure can only be mapped very coarsely. In Figure 8 we show two position–velocity diagrams (PVDs), roughly corresponding to the galaxy disk and tail. The disk pixels are defined to be those with $\Delta y \geqslant -1$ in Figure 7 and the tail pixels those with $\Delta y < -1$. We then extract PVDs as a

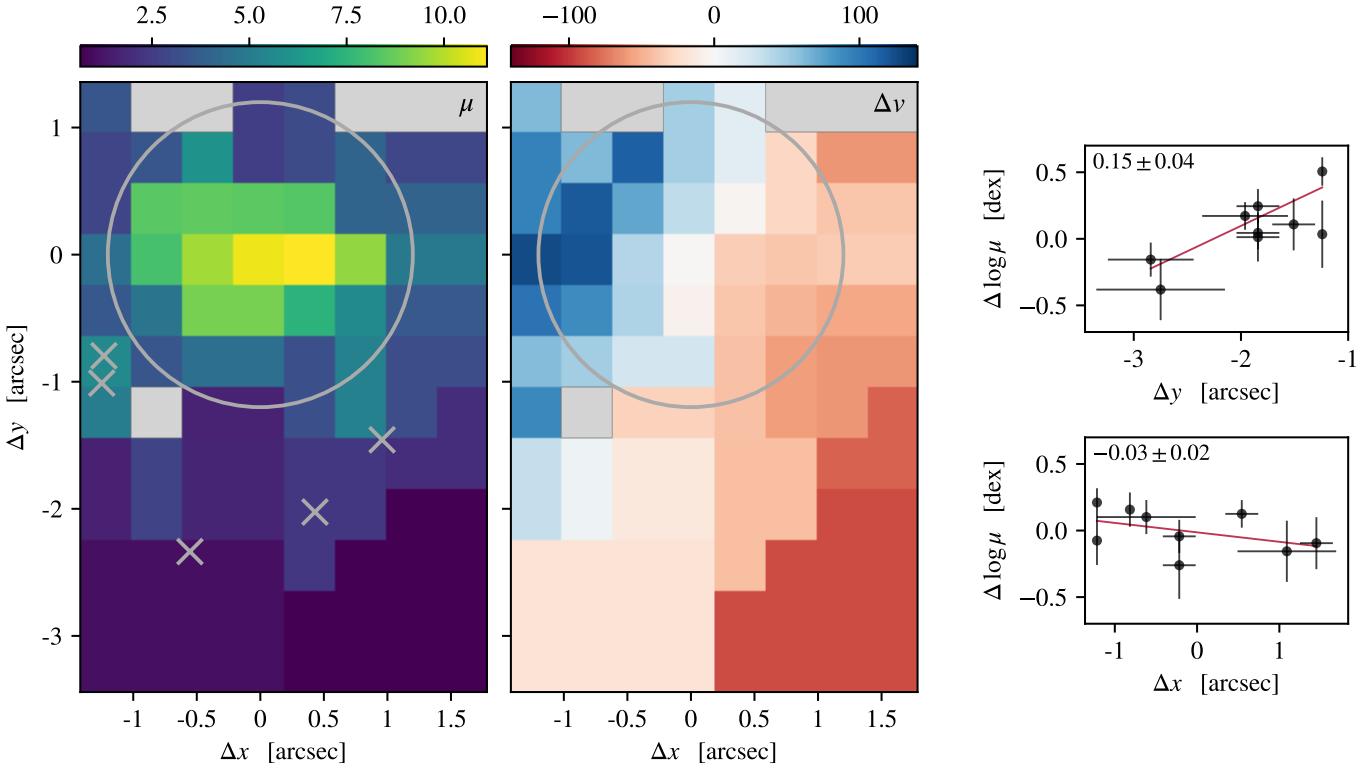

Figure 7. Maps of [O II] surface brightness and velocity for COSMOS2020-635829 (see Figure 4 for the orientation of the GMOS IFU). We only show spatial bins with [O II] detected at S/N > 3; undetected pixels and bins are shown in gray in each panel. The gray circle in each panel shows the extent of the main stellar disk ($2 \times r_e$), and the gray markers highlight the position of the JWST tail sources. Maps are in units of 10^{-17} erg s^{-1} cm^{-2} arcsec^{-2} and km s^{-1} for surface brightness and velocity, respectively. The right-hand panels show surface-brightness profiles (with arbitrary normalization) along the Δx- and Δy-directions. Each panel also shows the best-fit slope and uncertainty from a linear fit.

function of Δx, which roughly corresponds to the plane of rotation in the disk. Both PVDs show gradients consistent with rotation, with both showing similar slopes (at least given the small number of data points for the tail). There is an offset in systemic velocity between the disk and the tail of $\sim$50 km s^{-1}, as expected from Figure 6.

This is consistent with observations of jellyfish galaxies at $z \sim 0$, where ordered ionized gas rotation is almost always observed in the disk, and this rotation pattern is often also observable in regions of the tail as the stripped gas retains some of its orbital angular momentum as it is removed from the galaxy disk (e.g., M. Gullieuszik et al. 2017; B. M. Poggianti et al. 2017; A. Moretti et al. 2018; J. H. Lee et al. 2022; R. Luo et al. 2023).

5. Extraplanar Star Formation

Given the spatial coincidence between the ionized gas tail and the extraplanar JWST sources, and given the kinematic association between ionized gas tail and the main galaxy, we believe that these extraplanar optical and near-IR sources reflect sites of in situ star formation in an RPS tail. In this section we estimate the properties of these star-forming knots via SED fitting. We measure photometry within the four apertures shown in Figure 1. We note that "region 1" (and arguably "region 4") contains two peaks in the JWST imaging but we treat it as a single source since it is blended into a single source in the deconvolved Subaru imaging. The filters used are JWST F115W, F150W, F277W, and F444W, HST F814W, and Subaru *B*, *V*, *r*, and *z*. As mentioned in Section 2.1, we use the Subaru imaging from V. Sok et al. (2022), which is

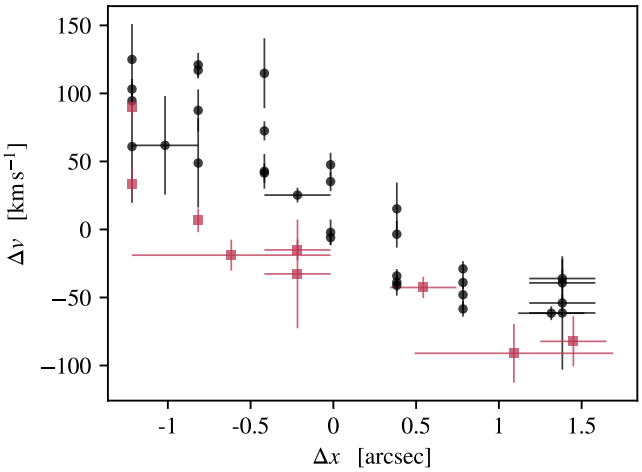

Figure 8. PVD along the Δx-direction from Figure 7. The main galaxy disk is shown by the black points and the tail is shown by the red points.

deconvolved to a resolution of 0.″3, and prior to measuring fluxes we also convolve the JWST and HST imaging to this resolution. We only include filters in the SED fitting where the flux is detected in the source aperture at $>5\sigma$. We determine the flux uncertainty by randomly positioning 1000 apertures (of equal size to the source aperture) across source-free regions in the image and measuring fluxes. We take the flux error to be the sigma-clipped standard deviation of the resulting aperture flux distribution. We note that the deconvolved *z*-band flux is undetected for all four sources.

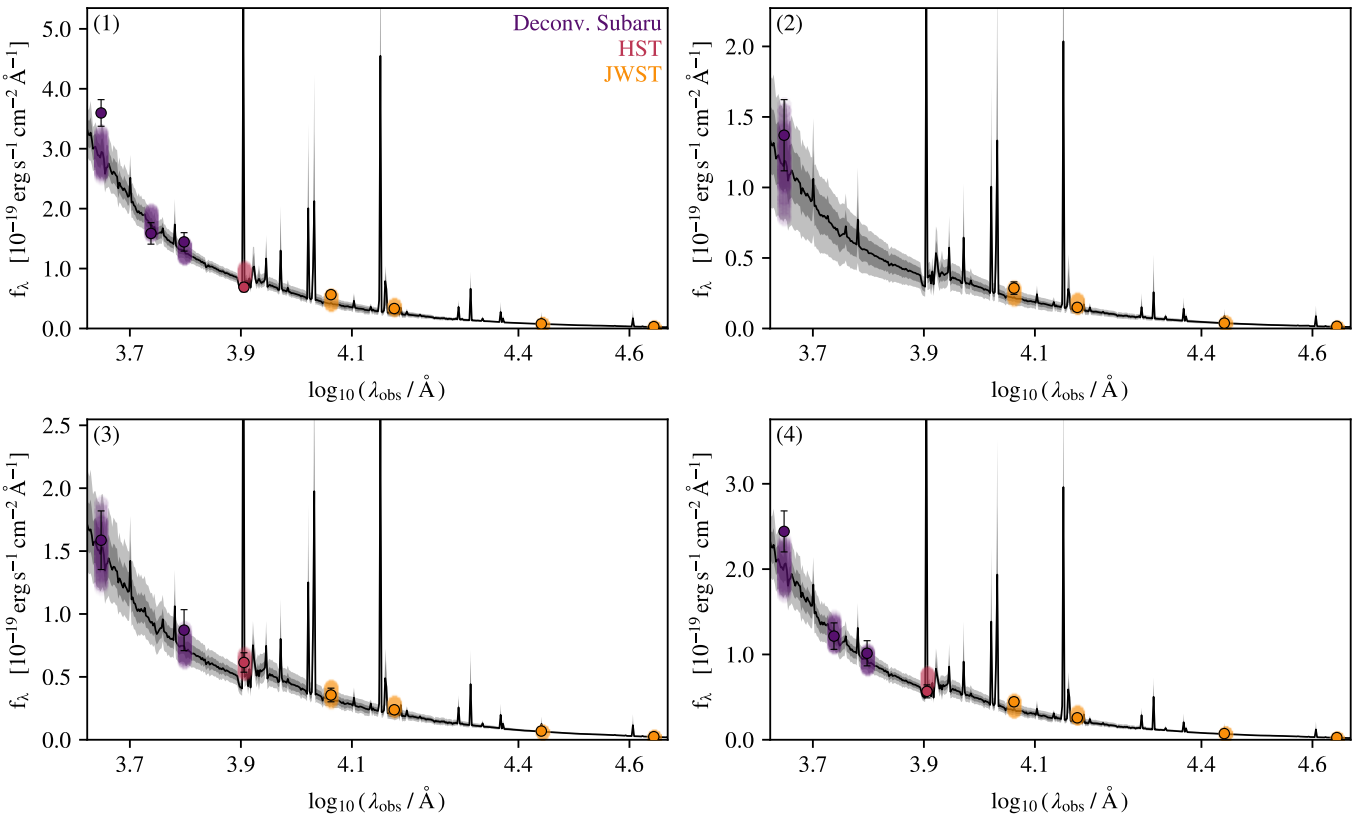

Figure 9. BAGPIPES SED fits for the four extraplanar sources identified in the tail of COSMOS2020-635829. Observed fluxes are shown by the data points. The solid black line shows the best-fit spectrum (50th percentile) and then gray shaded regions show the 68% and 95% credible regions. The colored bands show the 95% credible region for the expected flux in each of our observed filters, given the fitted model spectra. The region number (see Figure 1) is listed in the upper-left corner.

We perform SED fitting using the BAGPIPES code (A. C. Carnall et al. 2018, 2019) with the NAUTILUS sampler (J. U. Lange 2023). We assume a flexible continuity star formation history model and a Calzetti dust attenuation law (D. Calzetti et al. 2000). We use age bins of [0, 30, 90, 650, 1800, t_{max}] Myr, where t_{max} is the age of the Universe at $z = 1.156$. These bins correspond to a minimal and maximal age bin with approximately logarithmic time spacing in between. Dust A_V is allowed to vary freely between zero and two and metallicity between 0.01 and 2.5 × solar. We include a nebular emission component from CLOUDY (G. J. Ferland et al. 2017) with the ionization parameter fixed to $\log_{10}(U) = -3$ and fix the redshift to the spectroscopic redshift of COSMOS2020-635829.

In Figure 9 we show the SEDs for each of the tail sources alongside the best-fit spectrum from BAGPIPES. Immediately by eye it is clear that the photometry for all of the tail sources is consistent with a very young stellar population, both by the lack of a significant Balmer break and the steep UV slope. This is reinforced quantitatively in Figure 10 where we show the binned star formation histories from the SED fits. All sources are consistent with star formation exclusively within the past 100 Myr. The derived SFRs and stellar masses for each of the tail sources are listed in Table 1, where the listed SFRs correspond to averages over the past 100 Myr. Stellar masses are generally around $10^8\,M_\odot$ with SFRs that are a few tenths of a solar mass per year.

For further reference we also derive an integrated SFR for the main disk of COSMOS2020-635829 via SED fitting following the same procedure and using the same filters as for the tail sources (though the galaxy disk is detected in z band). We measure photometry for the disk in an aperture centered on the galaxy center with a radius of $2 \times r_e$. We estimate a log stellar mass (in solar masses) of $10.24^{+0.16}_{-0.07}$ and an SFR of $68^{+34}_{-18}\,M_\odot\,\mathrm{yr}^{-1}$, which are consistent with the COSMOS2020 values of $10.30^{+0.05}_{-0.07}$ and 71^{+22}_{-14}, respectively (J. R. Weaver et al. 2022). This means that the tail sources individually account for ∼1%–2% of the stellar mass of the main disk and ∼0.5% of the SFR (averaged over the past 100 Myr).

6. Discussion

6.1. Could COSMOS2020-635829 Be a Collisional Ring Galaxy?

As the knots in the tail of COSMOS2020-635829 are consistent with following a ringlike structure, here we will provide a relatively detailed discussion around whether the morphology of COSMOS2020-635829 could indicate a collisional ring galaxy (CRG) as opposed to RPS. Our ultimate conclusion is that we cannot rule out the possibility that COSMOS2020-635829 is a CRG, but we still favor RPS as the most likely driver of the observed stellar and ionized gas morphology for the reasons outlined below.

First and foremost, we consider the structure of the ionized gas tail shown in Figure 7. As noted in Section 4.2, there is a clear decrease in [O II] surface brightness from the galaxy disk to the edge of the IFU field along the y-axis, but there is no change in [O II] surface brightness in the tail along the x-axis. Conversely, ionized (and atomic) gas observations of ring galaxies show strong gas emission along the ring with a strong depression inside

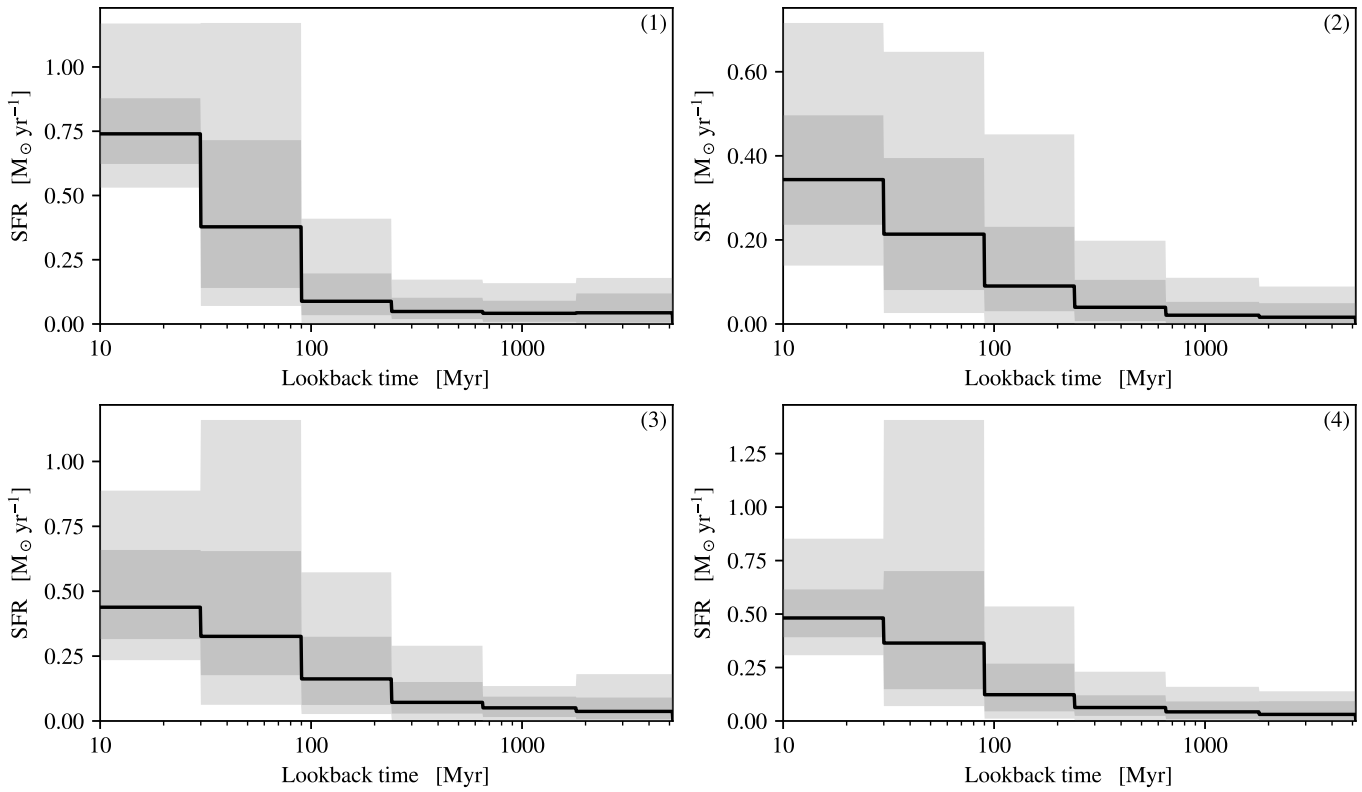

Figure 10. Star formation histories for the four extraplanar sources in the tail of COSMOS2020-635829. The star formation histories are determined from the SED fits shown in Figure 9. We use a flexible star formation history model with six logarithmically spaced age bins between 0 and ∼5 Gyr. The solid black line corresponds to the median star formation history and the shaded bands show the 84th and 95th percentile credible regions.

Table 1
Properties of the Tail Regions

ID	R.A. (deg)	Decl. (deg)	$\log_{10}(M_\star/M_\odot)$	SFR ($M_\odot$ yr^{-1})
1	149.81521	2.02786	$8.3^{+0.2}_{-0.4}$	$0.46^{+0.19}_{-0.12}$
2	149.81502	2.02747	$8.0^{+0.2}_{-0.3}$	$0.25^{+0.12}_{-0.09}$
3	149.81476	2.02761	$8.3^{+0.1}_{-0.2}$	$0.36^{+0.23}_{-0.11}$
4	149.81459	2.02775	$8.2^{+0.2}_{-0.2}$	$0.39^{+0.21}_{-0.13}$

of the ring (e.g., J. L. Higdon 1995, 1996; P. N. Appleton et al. 1999; I. Finkelman et al. 2011; J. L. Higdon et al. 2011; N. Deg et al. 2023; V. M. A. Gómez-González et al. 2024). Such a ring morphology is not at all indicated by Figure 7. Furthermore, ionized gas emission in CRG systems tends to be very bright along the ring structure and much fainter, or undetected, in the central galaxy (e.g., J. L. Higdon 1995; P. N. Appleton et al. 1999; I. Finkelman et al. 2011; L. Fogarty et al. 2011; V. M. A. Gómez-González et al. 2024). The opposite is true for COSMOS2020-635829: the [O II] emission peaks at the center of the galaxy and monotonically decreases along the tail direction.

Kinematically, it is difficult to distinguish between a CRG and an RPS tail, given the depth and, particularly, the angular resolution of our IFU data. In both cases we expect to see ordered rotation, especially for RPS when the axis of rotation in the disk is roughly perpendicular to the tail direction—as it is for COSMOS2020-635829. Some ring galaxies show kinematic misalignment, and even counterrotation, between the central galaxy and the ring (e.g., M. R. Merrifield & K. Kuijken 1994; A. Moretti et al. 2018; I. Y. Katkov et al. 2022; N. Deg et al. 2023), though this is not always the case (e.g., I. Finkelman et al. 2011). Regardless, we do not have sufficient angular resolution to determine whether or not there is kinematic misalignment between the galaxy and tail for COSMOS2020-635829. Though we can rule out counterrotation.

In terms of stellar morphology, at the very least, COSMOS2020-635829 does not seem to be a classical CRG with an outer ring clearly detached from the central galaxy (e.g., such as AM 0644-741 or Hoag's Object). Indeed, the compact knots detected by JWST can be traced back to the stellar disk via spiral arms extending from the eastern and western sides of the galaxy. It does bear mention that the Cartwheel galaxy shows spokes connecting the central galaxy to the outer ring (e.g., G. Hosseinzadeh et al. 2023). At $z \sim 0$, jellyfish galaxies show a wide range of stellar morphologies in their stripped tails. These include linear stellar streams, largely detached compact stellar knots, as well as relatively smooth, one-sided stellar extensions (e.g., L. Cortese et al. 2007; P. Jáchym et al. 2014; B. M. Poggianti et al. 2025), and COSMOS2020-635829 fits well within this diverse set.

Finally, we note that galaxies undergoing RPS and CRGs need not be mutually exclusive. There is at least one known example of a Hoag's-like ring galaxy being subsequently RPS, as presented in A. Moretti et al. (2018).

6.2. Implications for Ram-pressure Stripping

In this work we present evidence for the first RPS ionized gas tail at $z > 1$, which is found trailing to the south of the starburst galaxy COSMOS2020-635829 at $z = 1.156$. We also constrain for the first time the strength of extraplanar star

formation in a potential RPS tail at these redshifts. For this section, we make the assumption that the morphology of COSMOS2020-635829 is being driven by RPS, and then discuss the implications. While there are no direct comparisons for COSMOS2020-635829 at $z > 1$, we can compare the observed properties of COSMOS2020-635829 to jellyfish galaxies at lower redshift.

We first address the plausibility of RPS given the overdensities that COSMOS2020-635829 appears associated with (see Figure 2). The smaller ($\sim$few $\times$ 10^{13}) halo centered directly on COSMOS2020-635829 is, at best, marginally detected in X-rays with a luminosity of $8 \pm 6 \times 10^{42}$ erg s^{-1}, so while it may support a dense ICM we cannot say for sure. At this halo mass, such a system would have to be overbright in X-rays by roughly an order of magnitude in order to be detected at the above noise level (e.g., M. Sun 2012; Y.-L. Zheng et al. 2023; J. Braspenning et al. 2025). The large overdensity to the northeast of COSMOS2020-635829 has an X-ray luminosity of $2 \pm 0.5 \times 10^{43}$ erg s^{-1} (G. Toni et al. 2024) detected at 4σ. This X-ray luminosity is not dissimilar from values for massive groups and low-mass clusters at $z \sim 0$ (e.g., M. Sun 2012). Based on this X-ray luminosity we obtain an order-of-magnitude estimate for the corresponding ICM density of $\sim 10^{-27}$–10^{-26} g cm^{-3} for the inner regions of the halo (e.g., J. R. Peterson & A. C. Fabian 2006; M. Sun 2012). Even if the ICM density falls off by 1 or 2 orders of magnitude toward the outskirts of the halo, this still gives possible ram-pressure strengths of $\sim 10^{-11}$–10^{-14} g cm^{-1} s^{-2} for galaxy velocities between a few hundred and a thousand kilometers per second. These ram-pressure strengths are similar in magnitude to values estimated from observations of RPS in the local Universe and from hydrodynamic simulations (e.g J. E. Gunn & J. R. Gott 1972; D. Steinhauser et al. 2016; Y. L. Jaffé et al. 2018; I. D. Roberts et al. 2019; K. Yun et al. 2019; A. O. Broderick et al. 2025). Thus based on the X-ray data available for this system, there is no reason to exclude RPS as a perturbing force for COSMOS2020-635829. In fact, assuming that ICM profiles remain self-similar out to $z > 1$ (M. McDonald et al. 2017), then the strength of ram pressure (at fixed group or cluster mass) at these redshifts should be as strong, if not stronger, than at $z \sim 0$ (given the evolution in the critical density of the Universe). At some point this self-similarity likely breaks down at epochs where the ICM is still in the process of formation, though what redshift range this corresponds to is still uncertain.

At lower redshift, A. Boselli et al. (2019) detect striking 50–100 kpc RPS [O II] tails behind two satellite galaxies in an $\sim 10^{14}\,M_{\odot}$ cluster at $z \sim 0.7$. A. Boselli et al. (2019) find a typical [O II] surface brightness in the stripped tails of a few times 10^{-18} erg s^{-1} cm^{-2} arcsec^{-2}, whereas we find a typical [O II] surface brightness of $\sim 10^{-17}$ erg s^{-1} cm^{-2} arcsec^{-2}. The observed size of tail that we detect is far shorter than the tails found by A. Boselli et al. (2019), though for galaxy 345 in A. Boselli et al. (2019) the [O II] surface brightness within 10–20 kpc of the galaxy disk is close to the typical value that we find for COSMOS2020-635829. This may suggest that the intrinsic length of the ionized gas tail behind COSMOS2020-635829 is much longer than we observe, but this will require significantly deeper observations to constrain. At lower redshift, the largest compilation of [O II]-detected RPS tails is from A. Moretti et al. (2022) with $\sim$10 RPS galaxies in the A2744 and A370 clusters at $z \sim 0.3$–0.4. A new revelation from A. Moretti et al. (2022) is the fact that the ram-pressure tails in their sample show high [O II]-to-Hα ratios of 2–3, compared to typical galaxy disks with [O II]-to-Hα ratios less than unity. They argue that this anomalous ratio is either driven by the low gas densities in ram-pressure tails or is due to the complex interaction between the stripped tail and the surrounding ICM. At $z = 1.156$, the Hα line falls between the J and H bands and is thus unobservable from the ground for COSMOS2020-635829. So while we do not have constraints on the Hα emission for COSMOS2020-635829, these high [O II]-to-Hα ratios seen at intermediate redshifts may be aiding our ability to detect [O II] in the tail of COSMOS2020-635829 at $z > 1$. Moving forward, constraints on the Hα emission from COSMOS2020-635829 and its stripped tail will require spectroscopy from space.

In Figure 1 we highlight four extraplanar regions in the tail of COSMOS2020-635829 that are clear from the JWST imaging. We note that regions 1 and 4 are resolved into two sources in the JWST imaging but are blended into one in the deconvolved Subaru imaging that we use for SED fitting. These regions are blue in color and are consistent with exclusively young stellar populations formed within the past 100 Myr. Detached star-forming knots in Virgo Cluster ram-pressure tails tend to have stellar masses of $\sim 10^{3}$–$10^{5}\,M_{\odot}$ and SFRs of $\sim 10^{-4}$–$10^{-3}\,M_{\odot}$ yr^{-1} (J. A. Hester et al. 2010; M. Fumagalli et al. 2011; A. Boselli et al. 2021, 2022; Junais et al. 2021). For star-forming knots in the tails of jellyfish galaxies from the Gas Stripping Phenomena in Galaxies with MUSE (GASP) survey (B. M. Poggianti et al. 2017), stellar masses range between $\sim 10^{6}$ and $10^{8}\,M_{\odot}$ and SFRs between $\sim 10^{-4}$ and $10^{-1}\,M_{\odot}$ yr^{-1}. These can be compared to the typical stellar masses of $\sim 10^{8}\,M_{\odot}$ and SFRs of $\sim 0.3\,M_{\odot}$ yr^{-1} derived in this work for the four tail regions. These differences relative to the knots for Virgo galaxies are likely driven by the differences in physical resolution such that the JWST sources in regions in this work may correspond to multiple small sources blended together. Relative to $z \sim 0$, at $z \sim 1$ there is an increase by an order of magnitude in the normalization of the star-forming main sequence (SFMS; e.g., J. S. Speagle et al. 2014), which may also manifest itself in the specific SFR of detached star-forming knots. Relative to GASP sources, the physical properties of the four tail regions in this work are roughly consistent with the most massive GASP knots, though the SFRs for the regions in the tail of COSMOS2020-635829 are slightly larger (B. M. Poggianti et al. 2019). Incorporating the factor of $\sim$10 evolution in the SFMS moves the sources from this work well within the scatter of the GASP sample, though it remains to be seen whether this factor applies to star formation in stripped tails.

We can speculate on the fate of these extraplanar star-forming knots observed at $z > 1$. They may remain bound to the dark-matter halo of COSMOS2020-635829 and eventually be reaccreted on to the disk. The radial velocity offset of the tail relative to the main galaxy is modest at $\lesssim$50 km s^{-1}, but we cannot say whether this is indicative of a modest 3D velocity offset or a larger 3D velocity offset that is primarily in the plane of the sky. Simulations of isolated RPS find that most stars formed within 20 kpc of the disk will eventually fall back onto the galaxy (S. Tonnesen & G. L. Bryan 2012; N. Akerman et al. 2025), which is about the maximum separation that we observe for tail sources from the disk of COSMOS2020-

635829. Thus, at least based on simulations, this may be the most likely fate. Alternatively these knots are unbound from COSMOS2020-635829. In this scenario there are two broad possibilities, either they survive as a compact stellar collection or they are tidally disrupted and disperse. The latter would contribute to the building up the intracluster light (ICL) that is observed in clusters from $z \sim 0$ out to $z \gtrsim 1$ (e.g., Y.-T. Lin & J. J. Mohr 2004; Y. Jiménez-Teja et al. 2019; C. Burke et al. 2012; H. Joo & M. J. Jee 2023). Section 5 suggests that $\sim 10^8$–$10^9\,M_\odot$ of total stellar mass has formed in the wake of COSMOS2020-635829 over the past $\sim$100 Myr. Exactly how much ICL could be built up in this fashion over the history of the cluster will depend enormously on the statistical frequency of RPS, and specifically extraplanar star formation in ram-pressure tails. Hydrodynamic simulations predict that up to 30% of the ICL is built up by "intracluster star formation" in gas clouds stripped from infalling galaxies (E. Puchwein et al. 2010), which is analogous to the extraplanar star formation that we measure for COSMOS2020-635829. However, some simulation results suggest that this extraplanar star formation plays a much smaller role in ICL accumulation (S. Tonnesen & G. L. Bryan 2012; N. Akerman et al. 2025). The other possibility is that these sources are self-gravitating and remain as bound objects that become separated from COSMOS2020-635829. Such objects would, by definition, be dark-matter deficient. This notion of small "galaxies" forming within ram-pressure tails is not a new one and has been speculated on both via the lens of low-redshift observations as well as hydrodynamic simulations (e.g., B. M. Poggianti et al. 2019; V. Lora et al. 2024). The masses of the tail sources in this work are consistent with the masses of dwarf galaxies in clusters at $z \sim 0$, but we have limited information on their sizes. The SED fits in Section 5 are done at $0\farcs3$ resolution (limited by the deconvolved Subaru images), but it is clear from the JWST images in Figure 1 that the continuum sizes of these sources are smaller than this. We estimate intrinsic FWHM sizes for these tail sources of $\sim 0\farcs13 \approx 1$ kpc (see Appendix), corresponding to effective radii of $\sim$500 pc. Thus the size and stellar mass of continuum sources in the tail of COSMOS2020-635829 do coincide with typical values for dwarf galaxies in low-z clusters (e.g., J. Kormendy et al. 2009; F. R. Marleau et al. 2025), but the dynamical evolution of these sources from $z \sim 1$ to the present day is highly uncertain. Even if they do survive as bound objects, which is far from a given, they may end up looking very different than they do at $z > 1$.

Finally, we briefly discuss the current evidence for RPS at $z > 1$, beyond this work. K. Xu et al. (2025) present compelling evidence for RPS molecular gas tails in a few galaxies[9] that are part of a $z = 2.51$ protocluster with a mass of $\sim 10^{14}\,M_\odot$. If confirmed, this would show that RPS is truly operating all the way back to Cosmic Noon. The galaxies from K. Xu et al. (2025) are broadly of a similar stellar mass and SFR to COSMOS2020-635829, and like this work, the proposed ram-pressure tails are shown to be kinematically connected to the main galaxy. We do not have molecular gas observations of COSMOS2020-635829, and K. Xu et al. (2025) do not have resolved rest-frame optical spectroscopy, so any direct comparisons are limited. That said, these works highlight the potential multiwavelength nature of ram-pressure tails at $z > 1$, a fact that is already well known in the low-redshift Universe (e.g., A. Chung et al. 2007; H. Ebeling et al. 2014; B. M. Poggianti et al. 2017; A. Boselli et al. 2018; P. Jáchym et al. 2019; I. D. Roberts et al. 2021b; H. W. Edler et al. 2023; H. J. Souchereau et al. 20252025). Moving forward it will be extremely valuable to obtain multiphase observations of these high-redshift ram-pressure tails to further understand this process in the early Universe and make detailed comparisons to examples at late times. There is also more marginal evidence for RPS at $z > 1$ in the literature, which has often been limited by angular resolution. A. G. Noble et al. (2019) present possible molecular gas extensions for cluster galaxies at $z \sim 1.6$, which may be tracing RPS. More indirect inferences have also been made in favor of RPS in this redshift range (e.g., J. B. Nantais et al. 2017; M. L. Hamadouche et al. 2025), though in these cases it is more difficult conclusively associate the observed trends with specific quenching mechanisms.

[9] Here our discussion is primarily referring to galaxies "D4," "D5," and "D6" from K. Xu et al. (2025), which seem to be the most compelling examples.

7. Conclusions

In this work we present COSMOS2020-635829 as a candidate jellyfish galaxy undergoing RPS at $z = 1.156$. Given the paucity of direct evidence for RPS at $z > 1$, COSMOS2020-635829 represents an important new addition to the broader understanding of environmental quenching at these early times. The key takeaways from this work are the following.

1. COSMOS2020-635829 displays a relatively symmetric stellar disk accompanied by a trail of star-forming knots to the south of the main galaxy, as identified from multiband JWST imaging.
2. We detect an ionized gas tail detected via the [O II] $\lambda\lambda$3726, 3729 doublet that is cospatial with these extraplanar continuum sources and kinematically coherent with the main galaxy disk.
3. The star-forming knots in the tail have stellar masses of $\sim 10^8\,M_\odot$ and SFRs of $\sim 0.3\,M_\odot\,\mathrm{yr}^{-1}$, though it is possible that the values represent the total of smaller knots below our resolution level that are being blended together. In total, these sources account for roughly 1% of the stellar mass and SFR of the main galaxy disk.

This work highlights the powerful combination of depth and angular resolution afforded by JWST. This permits spatially resolved analyses in order to directly constrain the quenching mechanisms at work in the high-redshift Universe. COSMOS2020-635829 is now an important laboratory in this regard and efforts moving forward will be dedicated to confirming the nature of this galaxy via multiwavelength observations of the candidate ram-pressure tail presented in this work.

Acknowledgments

We thank the anonymous referee for their thoughtful report that has clearly improved the paper. I.D.R. acknowledges support from the Banting Fellowship Program. We thank the COSMOS-Web team for providing publicly available, science-ready data products. This work was enabled by observations made from the Gemini North telescope, located within the Maunakea Science Reserve and adjacent to the summit of Maunakea. We are grateful for the privilege of observing the Universe from a place that is unique in both its astronomical

quality and its cultural significance. This work is based in part on observations obtained at the international Gemini Observatory, a program of NSF NOIRLab, which is managed by the Association of Universities for Research in Astronomy (AURA) under a cooperative agreement with the U.S. National Science Foundation on behalf of the Gemini Observatory partnership: the U.S. National Science Foundation (United States), National Research Council (Canada), Agencia Nacional de Investigación y Desarrollo (Chile), Ministerio de Ciencia, Tecnología e Innovación (Argentina), Ministério da Ciência, Tecnologia, Inovações e Comunicações (Brazil), and Korea Astronomy and Space Science Institute (Republic of Korea). This work is based in part on observations made with the NASA/ESA/CSA James Webb Space Telescope. The data were obtained from the Mikulski Archive for Space Telescopes at the Space Telescope Science Institute, which is operated by the Association of Universities for Research in Astronomy, Inc., under NASA contract NAS 5-03127 for JWST. This research is based in part on observations made with the NASA/ESA Hubble Space Telescope obtained from the Space Telescope Science Institute, which is operated by the Association of Universities for Research in Astronomy, Inc., under NASA contract NAS 5–26555.

Facilities: Gemini:Gillett (GMOS), HST (ACS), JWST (NIRCam), Subaru (Suprime-Cam).

Software: Astropy (Astropy Collaboration et al. 2013), `Bagpipes` (A. C. Carnall et al. 2018), Matplotlib (J. D. Hunter 2007), Nautilus (J. U. Lange 2023), Numpy (C. R. Harris et al. 2020)

Appendix
Tail Source Size Estimate

As an illustrative example, we will consider the source(s) in region 1 (see Figure 1). This region clearly contains two sources resolved by the JWST images. To constrain the source sizes (and determine whether or not these are simply point sources) we make a small cutout around the sources in region 1 and fit the flux map with the sum of two 2D Gaussian distributions. Figure 11 (top) shows the average FWHM source size[10] for each of the four JWST filters. For reference we also plot λ/D corresponding to the diffraction-limited point-spread function (PSF) size. The sources are marginally resolved with FWHM sizes that are $\sim$1.5–3$\times$ larger than the diffraction-limited PSF. In Figure 11 (bottom) we plot "deconvolved sizes" as a function of wavelength, where the deconvolved size is given by

$$\theta_{\rm deconv} = \sqrt{\theta^2 - \theta_{\rm diff}^2}, \quad \text{(A1)}$$

where θ is the best-fit source FWHM and $\theta_{\rm diff}$ is the diffraction-limited FWHM. After "deconvolution" all filters agree on an FWHM source size of $0\farcs13 \approx 1$ kpc corresponding to an effective radius of $\sim$500 pc. The deconvolution is only formally valid if the underlying source distribution is well described by a symmetric 2D Gaussian (i.e., a Sérsic index of 0.5), but still provides an approximate estimate for the characteristic underlying source size.

[10] The best-fit FWHMs for the two sources are consistent with each other for all filters, and therefore simplicity we only show the average FWHM.

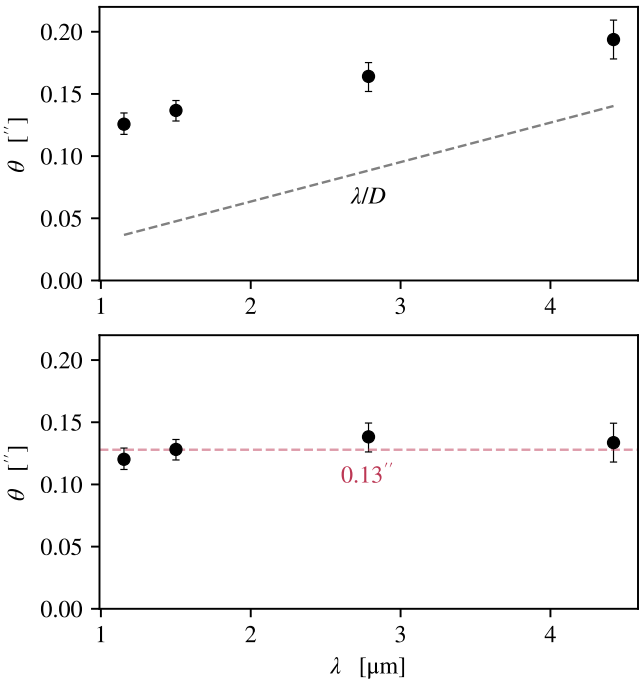

Figure 11. Size estimates for the extraplanar JWST sources in tail region 1. Top: best-fit Gaussian FWHM size averaged over the two JWST sources in tail region 1. Data points correspond to the four JWST filters. For reference we show the diffraction-limited PSF FWHM as a function of wavelength (dashed line), indicating that these sources are only marginally resolved. Bottom: deconvolved FWHM source sizes as a function of wavelength (see text for details).

ORCID iDs

Ian D. Roberts https://orcid.org/0000-0002-0692-0911
Michael L. Balogh https://orcid.org/0000-0003-4849-9536
Visal Sok https://orcid.org/0000-0003-0780-9526
Adam Muzzin https://orcid.org/0000-0002-9330-9108
Michael J. Hudson https://orcid.org/0000-0002-1437-3786
Pascale Jablonka https://orcid.org/0000-0002-9655-1063

References

Akerman, N., Tonnesen, S., Poggianti, B. M., et al. 2025, A&A, 698, A151
Appleton, P. N., Charmandaris, V., Horellou, C., et al. 1999, ApJ, 527, 143
Astropy Collaboration, Robitaille, T. P., Tollerud, E. J., et al. 2013, A&A, 558, A33
Balogh, Morris, S. L., Yee, H. K. C., Carlberg, R. G., & Ellingson, E. 1999, ApJ, 527, 54
Bellhouse, C., McGee, S. L., Smith, R., et al. 2021, MNRAS, 500, 1285
Blanton, M. R., & Moustakas, J. 2009, ARA&A, 47, 159
Boselli, A., & Gavazzi, G. 2006, PASP, 118, 517
Boselli, A., Fossati, M., Ferrarese, L., et al. 2018, A&A, 614, A56
Boselli, A., Epinat, B., Contini, T., et al. 2019, A&A, 631, A114
Boselli, A., Lupi, A., Epinat, B., et al. 2021, A&A, 646, A139
Boselli, A., Fossati, M., & Sun, M. 2022, A&ARv, 30, 3
Braspenning, J., Schaye, J., Pillepich, A., & Nelson, D. 2025, arXiv, arXiv:2511.09649
Broderick, A. O., Roberts, I. D., & Hudson, M. J. 2025, ApJ, 986, 132
Brown, T., Roberts, I. D., Thorp, M., et al. 2023, ApJ, 956, 37
Bureau, M., & Carignan, C. 2002, AJ, 123, 1316
Burke, C., Collins, C. A., Stott, J. P., & Hilton, M. 2012, MNRAS, 425, 2058
Calzetti, D., Armus, L., Bohlin, R. C., et al. 2000, ApJ, 533, 682
Cappellari, M. 2025, MNRAS, 544, 1432
Carnall, A. C., Leja, J., Johnson, B. D., et al. 2019, ApJ, 873, 44
Carnall, A. C., McLure, R. J., Dunlop, J. S., & Davé, R. 2018, MNRAS, 480, 4379
Casey, C. M., Kartaltepe, J. S., Drakos, N. E., et al. 2023, ApJ, 954, 31
Cerulo, P., Couch, W. J., Lidman, C., et al. 2016, MNRAS, 457, 2209

Chung, A., van Gorkom, J. H., Kenney, J. D. P., & Vollmer, B. 2007, ApJL, 659, L115
Copetti, M. V. F., & Writzl, B. C. 2002, A&A, 382, 282
Cortese, L., Marcillac, D., Richard, J., et al. 2007, MNRAS, 376, 157
Cortese, L., Boissier, S., Boselli, A., et al. 2012, A&A, 544, A101
Cortese, L., Catinella, B., & Smith, R. 2021, PASA, 38, e035
Crossett, J. P., Jaffé, Y. L., McGee, S. L., et al. 2025, A&A, 694, A204
de Propris, R., Stanford, S. A., Eisenhardt, P. R., Dickinson, M., & Elston, R. 1999, AJ, 118, 719
Deg, N., Palleske, R., Spekkens, K., et al. 2023, MNRAS, 525, 4663
DESI Collaboration, Adame, A. G., Aguilar, J., et al. 2024, AJ, 168, 58
Dressler, A. 1980, ApJ, 236, 351
Durret, F., Chiche, S., Lobo, C., & Jauzac, M. 2021, A&A, 648, A63
Ebeling, H., Stephenson, L. N., & Edge, A. C. 2014, ApJL, 781, L40
Edler, H. W., de Gasperin, F., Shimwell, T. W., et al. 2023, A&A, 676, A24
Faisst, A. 2024, COSMOS-Web (STScI/MAST)
Ferland, G. J., Chatzikos, M., Guzmán, F., et al. 2017, RMxAA, 53, 385
Finkelman, I., Moiseev, A., Brosch, N., & Katkov, I. 2011, MNRAS, 418, 1834
Finn, R. A., Desai, V., Rudnick, G., et al. 2018, ApJ, 862, 149
Finn, R. A., Rudnick, G., Jablonka, P., et al. 2025, ApJ, 985, 81
Fogarty, L., Thatte, N., Tecza, M., et al. 2011, MNRAS, 417, 835
Foreman-Mackey, D., Hogg, D. W., Lang, D., & Goodman, J. 2013, PASP, 125, 306
Franco, M., Casey, C. M., Koekemoer, A. M., et al. 2025, arXiv, arXiv:2506.03256
Fumagalli, M., Gavazzi, G., Scaramella, R., & Franzetti, P. 2011, A&A, 528, A46
Gavazzi, G. 1978, A&A, 69, 355
Gavazzi, G., & Jaffe, W. 1987, A&A, 186, L1
Gavazzi, G., Boselli, A., Mayer, L., et al. 2001, ApJL, 563, L23
Gómez-González, V. M. A., Mayya, Y. D., Zaragoza-Cardiel, J., et al. 2024, MNRAS, 529, 4369
Gullieuszik, M., Poggianti, B. M., Moretti, A., et al. 2017, ApJ, 846, 27
Gunn, J. E., & Gott, J. R., III 1972, ApJ, 176, 1
Haines, C. P., Pereira, M. J., Smith, G. P., et al. 2015, ApJ, 806, 101
Hamadouche, M. L., McLure, R. J., Carnall, A., et al. 2025, MNRAS, 541, 463
Harris, C. R., Millman, K. J., van der Walt, S. J., et al. 2020, Natur, 585, 357
Hester, J. A., Seibert, M., Neill, J. D., et al. 2010, ApJL, 716, L14
Higdon, J. L. 1995, ApJ, 455, 524
Higdon, J. L. 1996, ApJ, 467, 241
Higdon, J. L., Higdon, S. J. U., & Rand, R. J. 2011, ApJ, 739, 97
Hosseinzadeh, G., Sand, D. J., Jencson, J. E., et al. 2023, ApJL, 942, L18
Hu, D., Zaječek, M., Werner, N., et al. 2024, MNRAS, 527, 1062
Hunter, J. D. 2007, CSE, 9, 90
Ignesti, A., Vulcani, B., Botteon, A., et al. 2023, A&A, 675, A118
Jáchym, P., Combes, F., Cortese, L., Sun, M., & Kenney, J. D. P. 2014, ApJ, 792, 11
Jáchym, P., Kenney, J. D. P., Sun, M., et al. 2019, ApJ, 883, 145
Jaffé, Y. L., Poggianti, B. M., Moretti, A., et al. 2018, MNRAS, 476, 4753
Jiménez-Teja, Y., Dupke, R. A., Lopes de Oliveira, R., et al. 2019, A&A, 622, A183
Joo, H., & Jee, M. J. 2023, Natur, 613, 37
Junais, Boissier, S., Boselli, A., et al. 2021, A&A, 650, A99
Katkov, I. Y., Kniazev, A. Y., Sil'chenko, O. K., & Gasymov, D. 2022, A&A, 658, A154
Khostovan, A. A., Kartaltepe, J. S., Salvato, M., et al. 2026, ApJS, 282, 6
Kimm, T., Somerville, R. S., Yi, S. K., et al. 2009, MNRAS, 394, 1131
Kodama, T., & Arimoto, N. 1997, A&A, 320, 41
Koekemoer, A. M., Faber, S. M., Ferguson, H. C., et al. 2011, ApJS, 197, 36
Kormendy, J., Fisher, D. B., Cornell, M. E., & Bender, R. 2009, ApJS, 182, 216
Lange, J. U. 2023, MNRAS, 525, 3181
Larson, R. B., Tinsley, B. M., & Caldwell, C. N. 1980, ApJ, 237, 692
Lee, J. H., Lee, M. G., Mun, J. Y., Cho, B. S., & Kang, J. 2022, ApJ, 940, 24
Lin, Y.-T., & Mohr, J. J. 2004, ApJ, 617, 879
Lora, V., Smith, R., Fritz, J., Pasquali, A., & Raga, A. C. 2024, ApJ, 969, 24
Luo, R., Sun, M., Jáchym, P., et al. 2023, MNRAS, 521, 6266
Maier, C., Hayashi, M., Ziegler, B. L., & Kodama, T. 2019, A&A, 626, A14
Mancone, C. L., Gonzalez, A. H., Brodwin, M., et al. 2010, ApJ, 720, 284
Manuwal, A., & Stevens, A. R. H. 2023, MNRAS, 523, 2738
Marleau, F. R., Cuillandre, J. C., Cantiello, M., et al. 2025, A&A, 697, A12
Mayer, L., Mastropietro, C., Wadsley, J., Stadel, J., & Moore, B. 2006, MNRAS, 369, 1021
McConnachie, A. W., Venn, K. A., Irwin, M. J., Young, L. M., & Geehan, J. J. 2007, ApJL, 671, L33
McDonald, M., Allen, S. W., Bayliss, M., et al. 2017, ApJ, 843, 28
Merrifield, M. R., & Kuijken, K. 1994, ApJ, 432, 575
Moretti, A., Poggianti, B. M., Gullieuszik, M., et al. 2018, MNRAS, 475, 4055
Moretti, A., Radovich, M., Poggianti, B. M., et al. 2022, ApJ, 925, 4
Morgan, C. R., Balogh, M. L., Boselli, A., et al. 2024, A&A, 691, A20
Muzzin, A., Wilson, G., Yee, H. K. C., et al. 2012, ApJ, 746, 188
Muzzin, A., van der Burg, R. F. J., McGee, S. L., et al. 2014, ApJ, 796, 65
Nantais, J. B., Muzzin, A., van der Burg, R. F. J., et al. 2017, MNRAS, 465, L104
Noble, A. G., Muzzin, A., McDonald, M., et al. 2019, ApJ, 870, 56
Old, L. J., Balogh, M. L., van der Burg, R. F. J., et al. 2020, MNRAS, 493, 5987
Owers, M. S., Hudson, M. J., Oman, K. A., et al. 2019, ApJ, 873, 52
Peng, Y., Maiolino, R., & Cochrane, R. 2015, Natur, 521, 192
Peng, Y.-j., Lilly, S. J., Kovač, K., et al. 2010, ApJ, 721, 193
Peterson, J. R., & Fabian, A. C. 2006, PhR, 427, 1
Poggianti, B. M., Fasano, G., Omizzolo, A., et al. 2016, AJ, 151, 78
Poggianti, B. M., Moretti, A., Gullieuszik, M., et al. 2017, ApJ, 844, 48
Poggianti, B. M., Gullieuszik, M., Tonnesen, S., et al. 2019, MNRAS, 482, 4466
Poggianti, B. M., Vulcani, B., Tomicic, N., et al. 2025, A&A, 699, A357
Postman, M., Franx, M., Cross, N. J. G., et al. 2005, ApJ, 623, 721
Pradhan, A. K., Montenegro, M., Nahar, S. N., & Eissner, W. 2006, MNRAS, 366, L6
Puchwein, E., Springel, V., Sijacki, D., & Dolag, K. 2010, MNRAS, 406, 936
Quilis, V., Moore, B., & Bower, R. 2000, Sci, 288, 1617
Rasmussen, J., Ponman, T. J., & Mulchaey, J. S. 2006, MNRAS, 370, 453
Roberts, I. D., & Parker, L. C. 2017, MNRAS, 467, 3268
Roberts, I. D., & Parker, L. C. 2020, MNRAS, 495, 554
Roberts, I. D., Parker, L. C., Brown, T., et al. 2019, ApJ, 873, 42
Roberts, I. D., van Weeren, R. J., McGee, S. L., et al. 2021a, A&A, 652, A153
Roberts, I. D., van Weeren, R. J., McGee, S. L., et al. 2021b, A&A, 650, A111
Roberts, I. D., van Weeren, R. J., Timmerman, R., et al. 2022a, A&A, 658, A44
Roberts, I. D., Parker, L. C., Gwyn, S., et al. 2022b, MNRAS, 509, 1342
Roberts, I. D., van Weeren, R. J., de Gasperin, F., et al. 2024, A&A, 689, A22
Schaefer, A. L., Croom, S. M., Allen, J. T., et al. 2017, MNRAS, 464, 121
Schaefer, A. L., Croom, S. M., Scott, N., et al. 2019, MNRAS, 483, 2851
Scoville, N. 2006, Cosmic Evolution Survey ("COSMOS") (STScI/MAST)
Sok, V., Muzzin, A., Jablonka, P., et al. 2022, ApJ, 924, 7
Souchereau, Kenney, J. D. P., Jachym, P., et al. 2025, ApJ, 988, 72
Speagle, J. S., Steinhardt, C. L., Capak, P. L., & Silverman, J. D. 2014, ApJS, 214, 15
Steinhauser, D., Schindler, S., & Springel, V. 2016, A&A, 591, A51
Sun, M. 2012, NJPh, 14, 045004
Toni, G., Maturi, M., Finoguenov, A., Moscardini, L., & Castignani, G. 2024, A&A, 687, A56
Tonnesen, S., & Bryan, G. L. 2012, MNRAS, 422, 1609
van der Burg, R. F. J., McGee, S., Aussel, H., et al. 2018, A&A, 618, A140
Watts, A. B., Cortese, L., Catinella, B., et al. 2023, PASA, 40, e017
Weaver, J. R., Kauffmann, O. B., Ilbert, O., et al. 2022, ApJS, 258, 11
Wetzel, A. R., Tinker, J. L., & Conroy, C. 2012, MNRAS, 424, 232
Wetzel, A. R., Tinker, J. L., Conroy, C., & van den Bosch, F. C. 2013, MNRAS, 432, 336
Wilman, D. J., & Erwin, P. 2012, ApJ, 746, 160
Xu, K., Wang, T., Daddi, E., et al. 2025, arXiv, arXiv:2503.21724
Yagi, M., Yoshida, M., Komiyama, Y., et al. 2010, AJ, 140, 1814
Yun, K., Pillepich, A., Zinger, E., et al. 2019, MNRAS, 483, 1042
Zabel, N., Brown, T., Wilson, C. D., et al. 2022, ApJ, 933, 10
Zheng, Y.-L., Yang, X., He, M., et al. 2023, MNRAS, 523, 4909